applied sciences

MDPI

Article

Effects of External Cross-Frames on the Ultimate Behavior of a Twin Steel Trapezoidal Box-Girder Bridge

Janghwan Kim [1], Byeong Wan Kwon [2,*] and Seungwon Kim [1,*]

[1] Department of Civil Engineering, Kangwon National University, Samcheok-si 25913, Republic of Korea; janghwan.kim@kangwon.ac.kr
[2] Department of Energy Resource and Chemical Engineering, Kangwon National University, Samcheok-si 25913, Republic of Korea
* Correspondence: bwkwon@kangwon.ac.kr (B.W.K.); seungwon.kim@kangwon.ac.kr (S.K.); Tel.: +82-33-570-6549 (B.W.K.); +82-33-570-6511 (S.K.)

Abstract: In the construction of a twin-steel box-girder bridge, external cross-frames are temporarily used to increase torsional resistance. These members are regarded as secondary and are removed after a composite action in the bridge is achieved. Recently, attention has been paid to the possibility that external cross-frames can be a redundant source in bridges with girder fractures. In this study, the effects of external cross-frames on a damaged bridge were investigated using finite-element bridge models. Therefore, full-scale bridge models of a twin-steel trapezoidal box-girder bridge were constructed using K-type external cross-frames. Various failure modes, including the buckling and yielding of the cross-frames, were incorporated into the bridge models to account for realistic behaviors in the damaged bridge. The analysis results showed that the external cross-frames increased the load-carrying capacity of the bridge with one-girder fracture damage by transversely redistributing the live loads.

Keywords: external cross-frame; redundancy; ultimate capacity; bridge collapse; bridge safety

check for updates

Citation: Kim, J.; Kwon, B.W.; Kim, S. Effects of External Cross-Frames on the Ultimate Behavior of a Twin Steel Trapezoidal Box-Girder Bridge. *Appl. Sci.* **2023**, *13*, 8810. https://doi.org/10.3390/app13158810

Academic Editor: Carmelo Gentile

Received: 28 June 2023
Revised: 20 July 2023
Accepted: 27 July 2023
Published: 30 July 2023

Copyright: © 2023 by the authors. Licensee MDPI, Basel, Switzerland. This article is an open access article distributed under the terms and conditions of the Creative Commons Attribution (CC BY) license (https://creativecommons.org/licenses/by/4.0/).

1. Introduction

Twin-steel box-girder bridges are a popular bridge type frequently used for highway interchanges because of their aesthetically pleasing appearance and high torsional resistance. However, two-girder bridges have been classified as fracture critical bridges according to the AASHTO LRFD bridge design specifications [1], which implies that the failure of one girder leads to bridge collapse. Based on this classification, twin-steel box-girder bridges are required to meet stricter provisions than non-fracture-critical bridges, such as the mandatory use of high-fracture-toughness materials, biennial hands-on inspections, and nondestructive inspections of welded connections [2]. These restrictions not only increase construction and maintenance costs but also discourage bridge owners from adopting this type of bridge despite its structural efficiency. Meanwhile, there have been several past incidents involving the significant failure of bridge components in steel plate-girder bridges classified as fracture critical, such as the I-79 Glenfield Bridges [3], US 422 [4], and I-794 Hoan bridge [5]. In these incidents, the applied loads were redistributed to the integral parts of the bridges without collapse, which suggests that inherent redundancy could exist in two-girder bridges.

Various studies have been conducted to determine the redundancy sources in a two-girder bridge. Hartle et al. [6] proposed three different sources of redundancy for a bridge: internal, load-path, and structural redundancy. Dexter et al. [7] and Hunley and Harik [8] suggested that even a two-girder composite bridge could be redundant owing to internal load redistribution. Park et al. [9] and Abedin and Mehrabi [10] found that I-shaped cross beams could contribute to an increase in the ultimate loading capacity of a steel plate girder bridge with one-girder fracture damage. Williamson et al. [11] and Samaras

et al. [12] showed that the concrete deck of a twin-steel trapezoidal box-girder bridge could provide load path-type redundancy. In addition to the concrete deck, Pham et al. [13] found that the external cross-frames in a twin-steel box-girder bridge could contribute to load redistribution based on experimental tests.

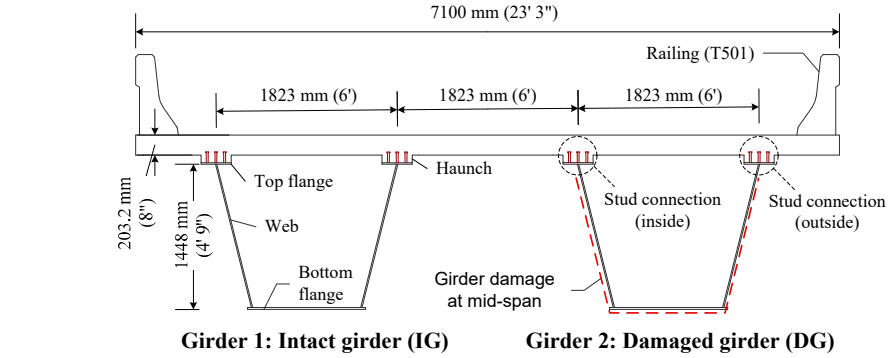
The external cross-frames in a twin-steel box-girder bridge have been neglected in redundancy evaluation because they are temporarily used during the bridge construction process. External cross-frames were installed between the steel girders, and the torsional resistance increased before the composite actions were obtained by casting a concrete deck [14,15]. This is a common process in which they are removed after bridge construction. Furthermore, they comprise of angles and T-sections that may be vulnerable to buckling by compressive forces in the ultimate behavior of the bridges. Therefore, they are regarded as secondary members and neglected in the redundancy evaluation of twin-steel box-girder bridges. If external cross-frames could improve the redundancy of bridges, they could be utilized to enhance bridge safety without changing design practices and increasing costs significantly.

In this study, the effects of K-type external cross-frames on the ultimate behavior of a twin-steel trapezoidal box-girder bridge were evaluated to investigate a possibility as the redundancy source of the bridge. For this purpose, finite element (FE) bridge models were constructed to simulate the possible failure modes of external cross-frame members, such as section yielding and buckling behaviors. In addition, various failure behaviors required for redundancy evaluation, such as large deflections, material inelasticity of concrete and steel, and stud connection failure, were incorporated into the models based on the modeling techniques proposed by Kim and Williamson [16]. It was assumed that one of the two girders was fully fractured, and truck live loads were applied to the damaged girder side to generate the maximum bending moment at the fracture location. To verify the validity of the FE models, the load-displacement response was compared with the full-scale bridge fracture test results obtained by Williamson et al. [11]. The verified models were utilized to evaluate the effects of external cross-frames. Analysis cases were determined depending on the potential failure modes of the frames. Based on these cases studies, guidelines were proposed for the external cross-frames.

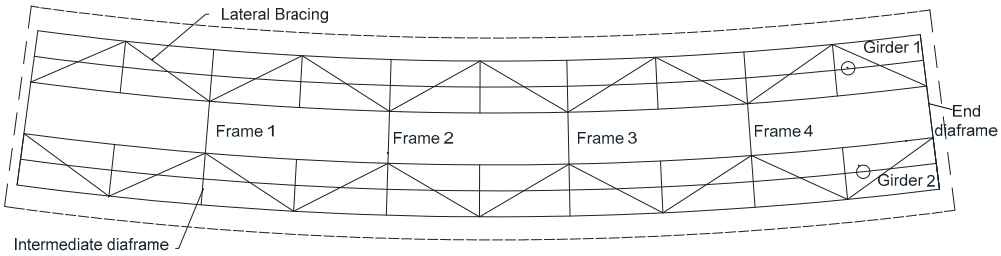
2. Prototype Bridge and Evaluation Scenario

2.1. Prototype Bridge

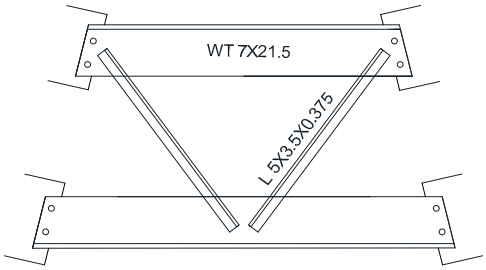
The prototype bridge, which is schematically shown in Figure 1a, comprised of two trapezoidal box girders and a concrete deck. The bridge was 36.58 m (120 ft), and it was simply supported. The depth and width of the girders were 1448 mm (4 ft, 9 in.) and 1823 mm (6 ft), respectively. The thickness of the concrete deck was 203.2 mm (8 in). The concrete deck was combined with steel girders using welded headed studs installed on the top flanges. Haunches (76.2 mm (3 in.)) were used to maintain a uniform deck thickness above the top flange. T501 safety rails were installed on top of the concrete deck with expansion joints every 9.14 m along the span direction. This bridge was slightly curved with a radius of curvature 416.2 m (1365 ft). External cross-frames were placed at four locations, as indicated in Frames 1–4 in Figure 1b. These cross-frames were temporarily installed to increase the rotational resistance during the erection of the bridge and were removed after casting the concrete deck and rails. As shown in Figure 1c, the external cross-frames comprised of top and bottom chords and two diagonals. WT 7X21.5 rolled sections were utilized for the chords and L 5X3.5X0.375 angles for the diagonals. The L-shaped angles were welded to the top and bottom chords. The external cross-frames were connected to WT 7X21.5 shapes with the flanges bolted to the webs of the bridge girders.



(**a**) Cross section



(**b**) Framing plan



(**c**) External cross-frame.

Figure 1. Schematic view of the prototype bridge.

2.2. Evaluation Scenario

The prototype bridge was utilized for a full-scale bridge fracture test program comprised of three different experiments depending on the damage levels and loading schemes [11]. In this study, a bridge fracture test result for the ultimate load-carrying capacity was utilized to evaluate the validity of FE bridge models. In this bridge fracture test, girder fracture damage was applied to one of the two girders at the mid-span of the bridge. After applying the girder fracture damage, concrete blocks and a load base simulating multiple truck live loads were applied. As shown in Figure 2a, concrete blocks were placed on the deck and transversely biased toward the fractured girder to induce a maximum positive bending moment at the fracture location. The weight of the blocks used to form the tub shape was 365 kN (82.1 kips). To match the loading points of the concrete blocks with the axles of a standard truck live load, wooden blocks were placed under the concrete blocks. A load base comprised of gravel and dirt was placed inside the tub to apply an additional load until the bridge collapsed. The standard truck live load was comprised of three axles. The front axle load was 36 kN (8 kips) and the middle and rear loads were 142 kN (32 kips). Note that the loading configuration in the bridge fracture test was different from the standard truck live load, although the concrete blocks and load base were intended to simulate multiple standard truck live loads by placing one truck on top of the other. When the total weight of the concrete blocks and load base reached 1614 kN (363 kips), the bridge collapsed, as shown in Figure 2b. The total weight

corresponds to approximately five-times the standard truck load (HS-20) specified in the AASHTO Bridge Design Specifications [1].

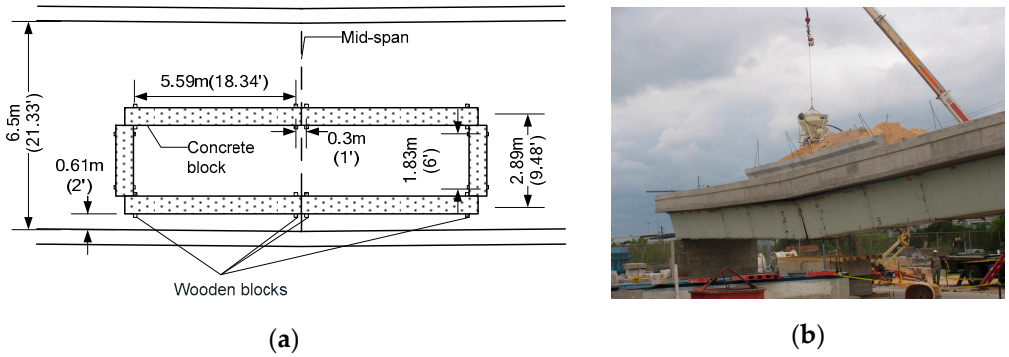


Figure 2. Loading configuration for the bridge fracture test. (**a**) Simulated load configuration. (**b**) Bridge fracture test (Williamson et al. 2010, [11]).

As aforementioned, the loading configurations of the live loads mimicked in the bridge fracture test differed from those of the standard truck live load. Therefore, two loading scenarios were used in this study. The first loading scenario followed the simulated loading used in the bridge fracture test. This loading scenario was used to verify the FE bridge models. For this loading configuration, the concrete blocks were modeled with point loads and gravel, including dirt with distributed loads, in the FE simulation. The other scenario followed the loading configuration of a standard truck live load. This scenario was used to evaluate the effects of the external cross-frame on the ultimate behavior of the bridge. In this scenario, the truck axle loads were modeled using point loads. To apply loads until the bridge collapsed, the axle loads were increased proportionally beyond the one-truck loading. Details of the FE models are described in the following section.

3. Numerical Modeling of Full-Scale Bridge

Full-scale FE bridge models based on the prototype bridge were constructed with various elements using ABAQUS/Standard 2021 [17], as shown in Figure 3. Steel plates, such as webs and flanges of girders were modeled using eight-node shell elements with reduced integration (S8R). The width ratios of the shell elements ranged between 1/7 and 1/4. Internal braces were modeled with a two-node truss (T3D2) and beam elements (B31), depending on the type connected to the webs of the girders: T3D2 elements for bolting connections and B31 for welding. The concrete deck and rails were modeled using eight-node solid elements with reduced integration (C3D8R). To avoid numerical errors caused by shape issues, the concrete and rails were meshed such that the maximum aspect ratio was within 3.5. The flexural reinforcement of the concrete deck and rails was modeled using two-node truss elements (T3D2). These elements were placed based on real positions, as in the prototype bridge. They did not share nodes with the solid elements for the concrete and rails. Instead, to maintain displacement compatibility, they were embedded into solid elements. In the prototype bridge, the haunches of the concrete deck were combined with the top flanges of girders using headed-welded studs. These connections were simplified by using connector elements (CONN3D2) in the bridge model. However, these elements contained specific load-displacement responses, including the effects of haunches under shear and tensile forces. Finally, the chord members of the external cross-frames were modeled with frame elements (FRAME3D) and diagonals with connector elements (CONN3D2). In the prototype bridge, the external cross-frames were connected to the webs of the girders using bolts. Therefore, the ends of the frame elements were attached to the girders using connector elements under hinge conditions.

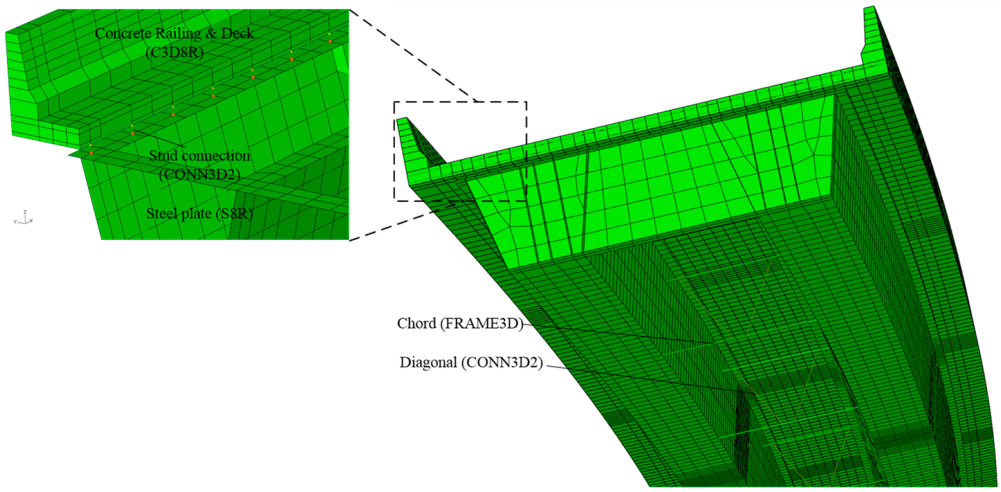


Figure 3. FE bridge model.

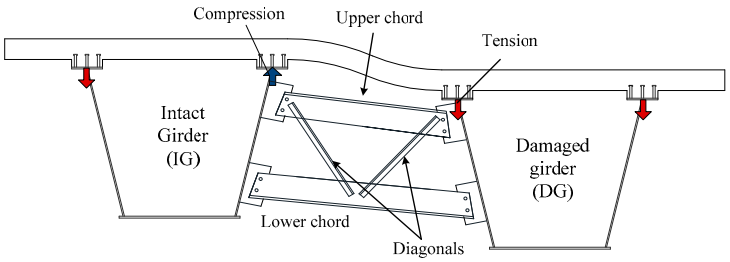
3.1. Material Non-Linearities and Stud Connection

Williamson et al. [7] reported that various failure modes could occur during a bridge fracture test for the ultimate loading capacity of a twin-steel trapezoidal box-girder bridge, such as the yielding of steel components and cracking and crushing of concrete. They also found that stud connection failure is an important feature related to the ultimate behavior of the bridge. Kim and Williamson [10,11] suggested modeling techniques for inelastic material behaviors and stud connection failure, and successfully evaluated the ultimate responses of a twin box-girder bridge with one girder fracture. They applied classical metal plasticity to steel and cast-iron plasticity to concrete components to account for material inelasticity.

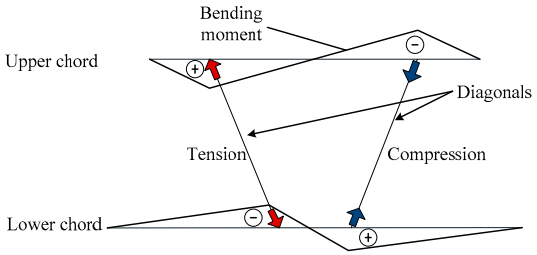
The stud connections are typically modeled as rigid ties [18,19] or nodal constraints [20,21] without considering potential failure. Under an undamaged condition, these modeling approaches give reasonably good results in the load-displacement estimation of a composite bridge. From the full-scale bridge fracture test, however, it was found that the stud connection failure could affect the ultimate behavior of the bridge. Based on this test result, Kim and Williamson [22] proposed a modeling method based on the results of stud pull-out tests conducted by Mouras [23] and Sutton [24]. In this method, the shear and tension failure modes of stud connections could be accounted for by including the interaction effect. In this study, the techniques proposed by Kim and Williamson [16,22] were utilized for the material nonlinearities and stud connection failures.

3.2. External Cross-Frame

The external cross-frames used in the prototype bridge were K-type, as shown in Figure 1). It comprised of WT 7 × 21.5 rolled sections for the upper and lower chords and L 5 × 3.5 × 0.375 angles for the diagonals. It was assumed that one of the two girders was fully fractured at its mid-span, and truck live loads were applied to the damaged side girder. Under these damage and loading conditions, transverse bending can occur to transfer the applied loads from the damaged girder to the intact girder, as shown in Figure 4a. As the external cross-frames were attached to the girders, it was presumed that they could resist the deformation of the damaged girder and contribute to the load transfer. Figure 4b shows the expected section forces of the external cross-frames caused by transverse bending. High bending moments can occur in the chord members, and a compression or tension force can develop in the diagonal members.



(**a**) Load transfer by transverse bending



(**b**) Expected section forces of the external cross-frame

Figure 4. Load transfer by transverse bending.

Potential failure modes of the WT section under flexure are material yielding, lateral torsional buckling, and local buckling. These failure modes could be simulated with fine meshes and material inelasticity. Note that the full-scale bridge modeling was constructed in this study, so it would not be efficient to apply fine meshes to detect the local failure modes of the frames. Furthermore, the local failure such as the buckling of the frames could introduce numerical ill-conditioning and difficulty in conversing to a solution. In this study, therefore, these potential failure modes were not directly simulated in the FE analysis. Instead, the nominal flexural strength of the WT section was calculated based on AISC 360-16 [25] and used as an upper limit of the frame elements (FRAME3D) for the chord members. The WT 21 × 21.5 used in the prototype bridge comprised of a compact flange and stem. The yield strength and elastic modulus of the WT section were 248 MPa (36 ksi) and 200 GPa (2900 ksi), respectively. The longest unbraced length (L_b) was 1943 mm (76.5 in.) in the upper chord member, which was less than the limiting laterally unbraced length (L_p) specified in the AISC 360-16 sect. F9, as indicated in Equation (1). Therefore, the flexural strength of the chord was governed by the yield of the entire section and was calculated as 28.7 kN-m (253.8 kip-in.) based on the plastic moment (M_p) in Equation (2). Once the section force of a flexural member reaches its plastic moment, a plastic hinge forms. Therefore, perfect plastic behavior was assumed in the FE simulations for the chord members beyond the plastic moment:

$$L_p = 1.76 r_y \sqrt{\frac{E}{F_y}} \tag{1}$$

$$M_p = F_y Z_x \tag{2}$$

where r_y is the radius of gyration about the y axis, E is the elastic modulus, F_y is the yield strength, and Z_x is the plastic section modulus about the x(strong) axis.

The diagonal members of the external cross-frame were modeled using connector elements (CONN3D2). The single angles used for the diagonals were under compressive or tensile forces and, therefore, could fail by tensile yielding, flexural buckling, and(or) torsional buckling. Similar to the chord members, the failure of the L 5 × 3.5 × 0.375 angles was simulated with nominal strength based on the AISC specification. The yield strength and elastic modulus of the diagonals were identical to those of the chord members.

Therefore, diagonal tensile failure occurred at 488 kN (109.8 kips). The compressive strength of an angle was calculated according to the provisions specified in AISC 360-16 sect. E5. The longer legs of the angles were welded to the chord members. The length of the angle L, was 1524 mm (60 in.). To account for the bending caused by load eccentricity, the AISC specifications allow the use of a modified effective slenderness, as indicated in Equation (3), for unequal leg angles. The radius of gyration r_a, for the angle about the geometric axis parallel to the connected leg was 25.9 mm (1.02.) Therefore, the modified effective slenderness ratio, L_c/r, was 116.1 based on Equation (3). The compressive strength P_c, of the angle was 240 kN (54 kips) based on Equations (4) and (5) for flexural buckling with a modified effective slenderness ratio:

$$\frac{L_c}{r} = 72 + 0.75\frac{L}{r_a} \text{ for } \frac{L}{r_a} \leq 80 \tag{3}$$

$$P_c = F_{cr}A_g \tag{4}$$

$$F_{cr} = \left(0.658^{F_y/F_e}\right)F_y \tag{5}$$

where L/r is the modified slenderness ratio, r_a is the radius of gyration about the geometric axis parallel to the connected leg, L is the length of the member, A_g is the cross-section area of the member, and F_e is the elastic buckling stress.

The tensile and compressive responses of the diagonal members were modeled using a simplified load-displacement behavior. As schematically shown in Figure 5, the effects of the limit states and post-failure behaviors under tension and compression were incorporated into the load-displacement behavior. The compressive and tensile strengths were determined using the nominal strengths specified in AISC 360-16 as aforementioned. Under tension, it was assumed that perfectly plastic behavior occurred beyond a displacement, δ_y, corresponding to the yield strength P_t, considering the ductility of the steel. For compression, it was assumed that the resistance decreased linearly after the buckling strength, P_c.

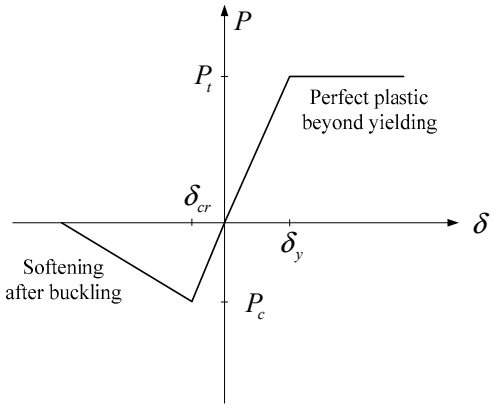


Figure 5. Load-displacement behavior of a diagonal member.

3.3. Verification of Numerical Model

The accuracy of the FE bridge models was verified by comparing the load-displacement response with full-scale bridge fracture test results for the ultimate load-carrying capacity conducted by Williamson et al. [11]. The verification model was simulated using material properties and loading configurations in accordance with the full-scale bridge fracture test. In the test, the compressive strength of the concrete members was 35.3 MPa (5.1 ksi). The yield strengths of the steel plates and reinforcements were 382 MPa (55.4 ksi) and 440 MPa (63.8 ksi), respectively. The external cross-frames were removed before girder damage was applied in the simulation, as in the bridge fracture test. The fracture damage was simulated by producing duplicate nodes of shell elements along a predefined fracture

path following the girder fracture line. The duplicate nodes were initially combined using connector elements under welding conditions, and the connector elements were removed before applying a live load to simulate the fracture.

In the bridge fracture test, concrete blocks were placed on wooden blocks, as shown in Figure 2a, and load bases, such as gravel and dirt were poured into a tub made of concrete blocks until the bridge collapsed. To match the loading configuration used for the test, the concrete blocks and load base were modeled with point and distributed loads, respectively. Figure 6 compares the load-displacement results of the test and simulation measured 5.49 m away from the midspan. The test results are plotted with a dotted line, and the simulation with a solid line. The load-displacement responses show a somewhat different pattern as the applied load reaches approximately 2.5-times the HS-20 truck live load. The test bridge show a sudden deflection increase as indicated by a plateau in the displacement response. This sudden deflection was caused by the stud connection failure in the outside of the fractured girder. Note that the test bridge was utilized for a series of fracture tests, such as bottom flange fracture and abrupt girder fracture, with one HS-20 truck load before the test for the ultimate load-carrying capacity considered in this study. It was presumed that this discrepancy was caused by the inherent stud connection damage that occurred during the previous two tests. As the applied load reaches about 1619 KN (364 kips), the test bridge was collapsed by the entire stud connection failure along the damaged girder. The overall response of the simulation agreed well with that of the ultimate load-carrying capacity test. The maximum capacity estimated from the FE simulation was 1638 kN (368.3 kips), which is approximately a one percent difference from the test.

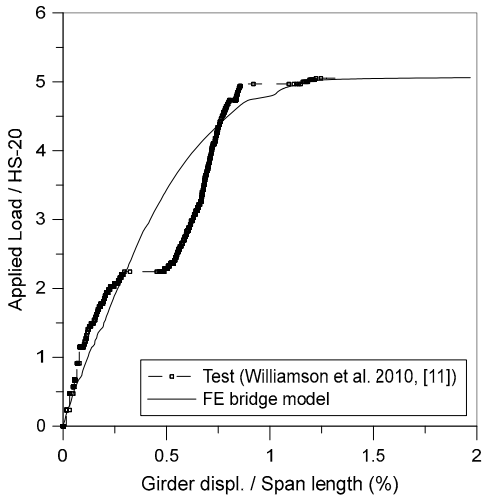


Figure 6. Load-displacement responses of fractured girder [11].

4. Effect of External Cross-Frame on Bridge's Ultimate Behavior

The external cross-frames of the prototype bridge were comprised of upper and lower chords and two diagonals, as shown in Figure 1c. The chords were made of WT 21 × 21.5 rolled sections and diagonals were made of L 5 × 3.5 × 0.375 angles. Four cases were investigated to evaluate the effects of an external cross-frame on the ultimate behavior of the bridge. In Case 1, the cross-frames were excluded as a basis for comparison with cases with cross-frames. In Case 2, the predicted failure modes of the cross-frame members, such as section yielding of the chords and yielding and buckling of the diagonals, were incorporated. In Case 3, the yielding and buckling of the diagonals were not considered; instead, an elastic behavior was assumed. This was intended to simulate a case in which sections heavier than L 5 × 3.5 × 0.375 angles were used, such that the diagonals did not fail before the plastic hinge formation of the chords. In Case 4, an elastic behavior was assumed for the chords. This case was considered to simulate a case in which the diagonals failed before the chords failed by applying sections heavier than the WT 21 × 21.5.

The material properties and simulation procedure of the FE bridge models were the same as those used for the verification. However, live loads with the configuration of the standard HS-20 truck were applied instead of the simulated truck loads used for verification. Full-depth girder fracture damage was applied at the midspan of one of the two girders. Live loads in the configuration of an HS-20 truck were then applied on top of the fractured girder. The middle axles of the truck were placed above the fracture damage and 0.61-m (2-ft) away from the railing to induce the maximum bending moment at the fracture location. As described in Section 2.2, the axle loads of the HS20 truck increased proportionally until the bridge collapsed.

4.1. Girder Displacement Responses

Figure 7 shows the load-displacement responses after one girder fracture was applied at the midspan. In Case 1, the ultimate load-carrying capacity was approximately 3.85-times of the HS-20 truck. This capacity was less than that estimated in the verification analysis. This discrepancy could be caused by differences in the live-load configurations. As mentioned in Section 2.2, the simulated live loads used for verification were modeled with point loads and distributed loads corresponding to the test setup. However, for these analysis cases, point loads matching the HS-20 truck were used, and thereby, a higher loading effect than the simulated loads was exerted. The collapse in Case 1 was initiated by the pullout failure of the stud connections in the fractured girder; therefore, the bridge lost the load-transferring resistance exerted by the concrete deck.

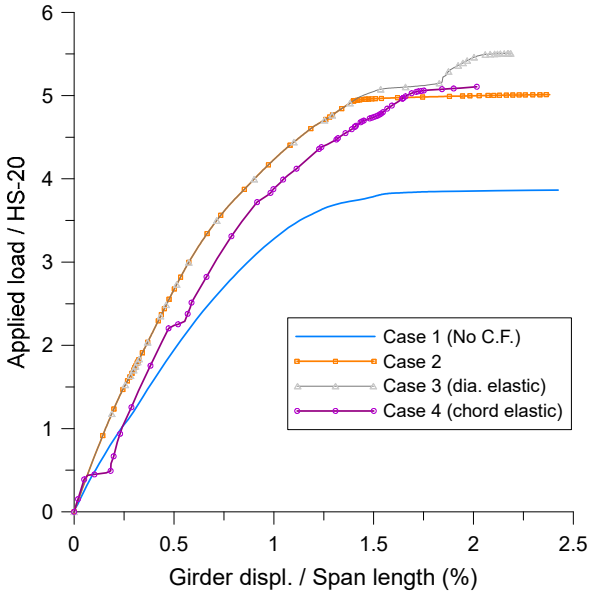


Figure 7. Load-displacement responses at midspan.

The cases with external cross-frames (Cases 2–4) resulted in a higher load-carrying capacity than that in Case 1. Case 2 exhibited approximately five-times the ultimate capacity of an HS-20 truck. Case 3 showed a similar load–displacement behavior as Case 2, but its capacity (5.46-times of the HS-20 truck) was 9.2% higher than that of Case 1. This discrepancy may be caused by the buckling effect of the diagonal. In Case 2, the right diagonal member of the external cross-frame near the midspan (Frames 2 and 3) buckled as the applied load reached its maximum capacity. Therefore, the external cross-frame loses its resistance to transverse external loads. Meanwhile, the elastic behavior of the diagonals was assumed in Case 3; therefore, the external cross-frames could provide resistance beyond the ultimate load estimated in Case 2.

Case 4 exhibited somewhat complicated behaviors compared to the other cases, although its ultimate capacity was similar to that of Case 2 (5.09-times of the HS-20 truck). As the normalized load reached approximately 40% of the HS-20, girder displacement

suddenly increased. This tendency was repeated when the applied load reached approximately 2.2-times of the HS-20 truck. Considering that the chords behaved elastically in Case 4, the expected failure mode was buckling of the diagonals. Therefore, these sudden increases could be attributed to buckling as the applied load increased. Further details on the members of the cross-frames are provided in the following section.

4.2. Section Forces of External Cross-Frame

As described in Section 3.2, it was expected that the external cross-frame would contribute to the transfer of live loads from the fractured girder to the intact girder after one girder fractures. The analysis results shown in Figure 8 correspond to the expected behavior induced by this load transfer mechanism. The compressive force developed on the right-side diagonal, and the tensile force on the left diagonal. In the upper chord, a negative bending moment occurred where the right-side diagonal (dia_R) was connected, and a positive bending moment occurred where the left-side diagonal (dia_L) was connected, as shown in Figure 8a. Reverse bending moments occurred in the lower chord, as shown in Figure 8b.

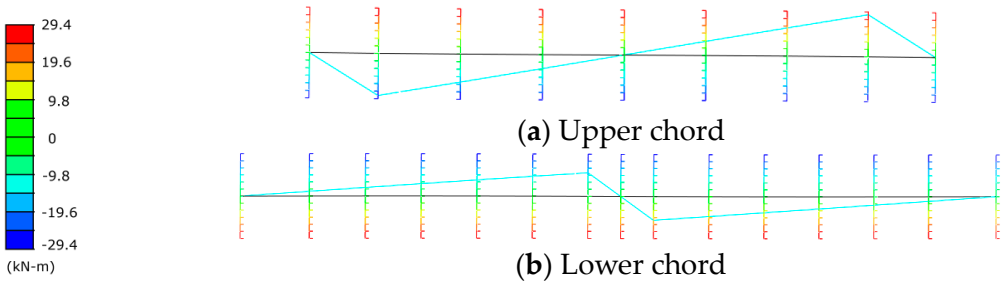


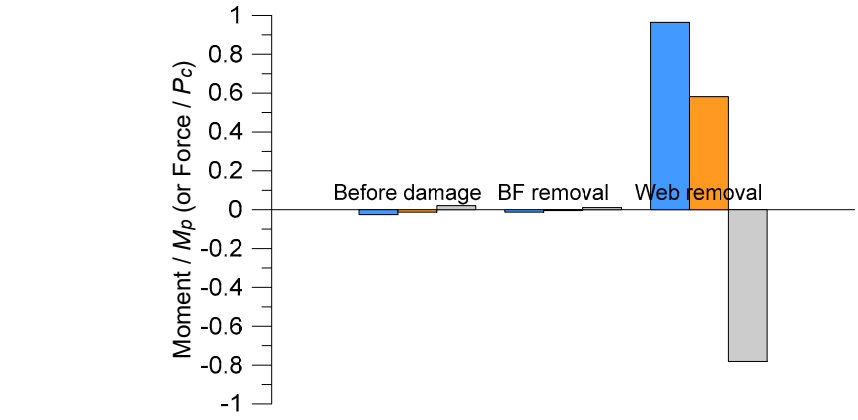
Figure 8. Bending moment of chords in Frame 2 (SM1).

Figure 9a shows the maximum section force variations in Frame 2 along the damage level in Case 2. The bending moments normalized by the flexural strength M_p are plotted with blue and orange bars for the upper and lower chords, respectively. The compressive axial force normalized by the buckling strength P_c, on the right-side diagonal (dia_R) is indicated by the gray bars. Figure 9b,c show the normalized section force variations of the chords and diagonals along the live loads after girder fracture. In Figure 9b, the solid blue and dashed orange lines indicate the bending moments of the upper and lower chords, respectively. The compressive force on the right diagonal (dia_R) is plotted with a solid line, and the tensile force on the left diagonal (dia_L) is plotted with a dashed line.

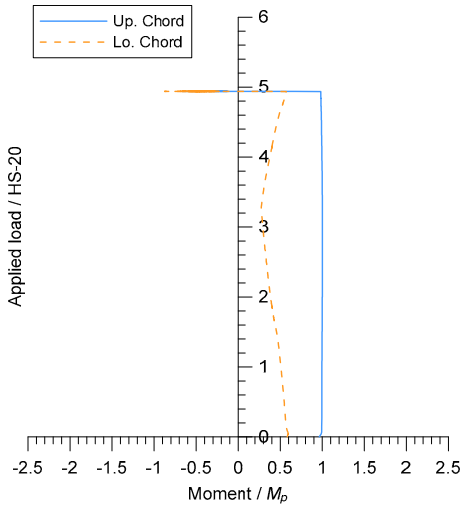
As shown in Figure 9a, the section forces did not vary significantly until the bottom flange fractured; however, they increased as web fracture damage was applied. With the web fracture, the bending moment increased to 96% of the flexural strength in the upper chord. As the live loads increased, the normalized bending moment of the upper chord readily reached one and, therefore, it was presumed that a plastic hinge formed at that location. The compressive force on the right-side diagonal (dia_R), as shown in Figure 9c, increased and reached its buckling strength when the applied live load exceeded approximately five-times that of the HS-20 truck. At this stage, the cross-frame lost its resistance to laterally transferring live loads from the fractured girder to the intact girder. Therefore, the axial forces suddenly decreased, as shown in Figure 9b,c. This tendency conforms to the load-displacement behavior described in the previous section.

Figure 10 shows the axial force variations of the diagonals for Cases 2–4 after the girder fracture. The dashed and solid gray lines indicate the axial forces of the left-side diagonals (dia_L) and right-side diagonals (dia_R) of Frame 2, respectively. The axial forces of Frame 1 are plotted as dashed orange lines for dia_L and solid orange lines for dia_R. Before applying live loads, the section force of dia_L was compression and that of dia_R was tension in Frame 1, which was the opposite of that in Frame 2. This can be attributed to the extensive downward girder deflection of the right-side girder. The fractured girder

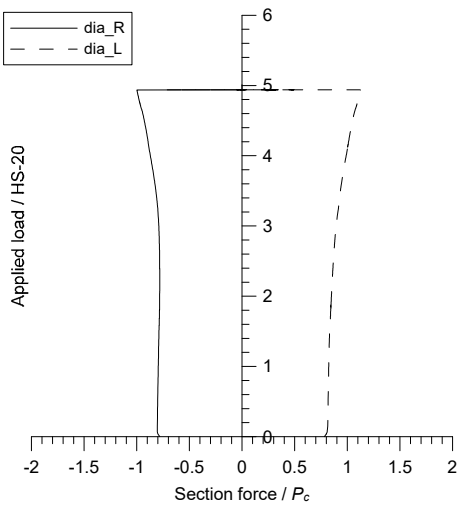
was discontinuous at the midspan due to the fracture of the girder, which caused extensive girder rotation. To resist such girder displacement, downward reactions occurred at the support of the fracture girder while leaving local upward deflection near Frame 1. However, this tendency disappeared as the live loads increased and reverted to the same pattern as that in Frame 2. As shown in Figure 10a,b, the loaded pattern of Case 2 was similar to that of Case 3. Initially, Frame 2 transferred only the live load from the fractured girder to the intact girder. However, as the live loads exceeded 1.35-times of the HS-20 truck, Frame 1 began to be involved in the load transfer. In Case 2, the bridge collapse was initiated by the buckling of the diagonal of Frame 2, as the applied live loads reached approximately five-times the HS-20 truck load. In Case 3, elastic behavior was assumed for the diagonals; therefore, the bridge sustained higher loads than those in Case 2. However, bridge collapse occurred when the applied live loads reached 5.5-times the HS-20 truck. The collapse was initiated by the extensive concrete failure of the concrete deck. In Case 4, the elastic behavior of the chords was assumed. As shown in Figure 10c, the diagonals of Frame 2 and Frame 1 buckled sequentially as the applied load reached approximately 0.4-times and 2.2-times of the HS-20 truck, respectively. After the diagonals under compression buckled, the external cross-frame still resisted the applied live loads, and the bridge collapsed as the applied live loads reached approximately 5.1-times of the HS-20 truck. Further details of the collapse patterns are discussed in the following section.



(**a**) Section forces along damage



(**b**) Bending moment of chords



(**c**) Axial forces of diagonals

Figure 9. Section forces of Frame 2 (Case 2).

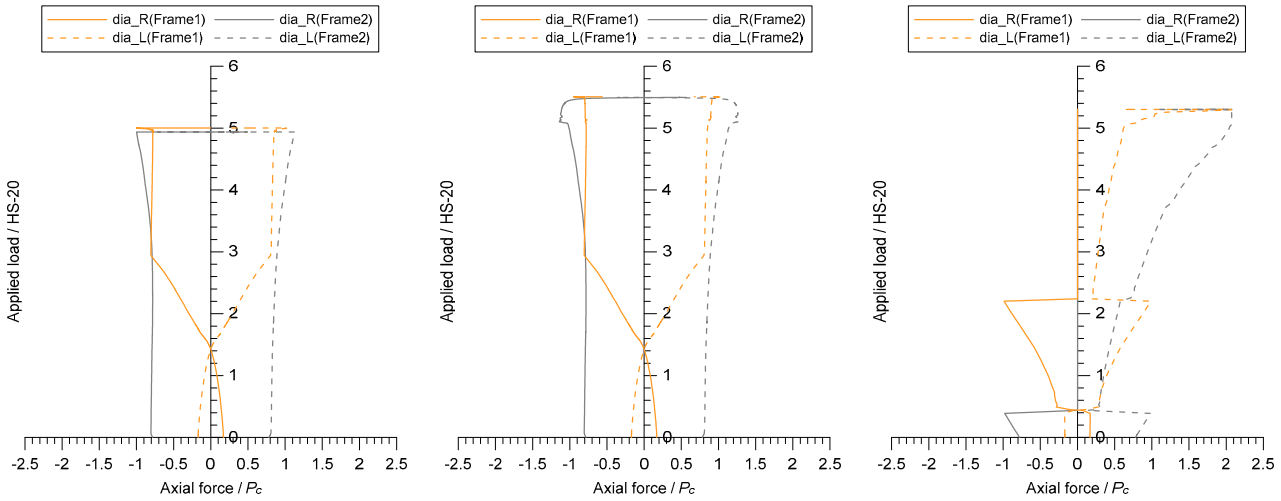
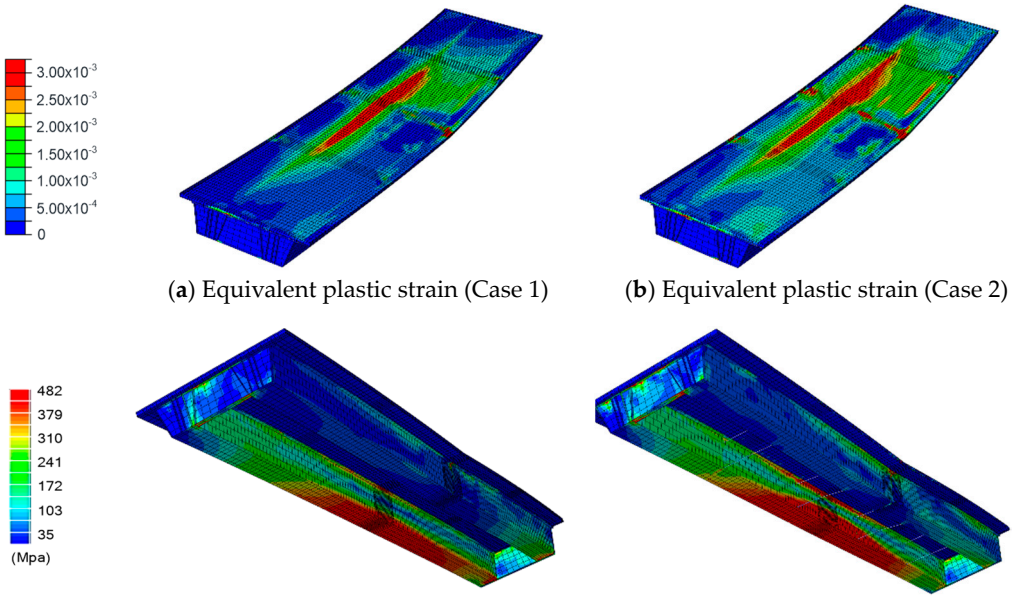


Figure 10. Axial forces of diagonals.

4.3. Collapse Patterns

Figure 11 shows the equivalent plastic strains and Von Mises equivalent stresses as the applied loads reached the ultimate capacities in Cases 1 and 2. As aforementioned, the bridge without the external cross-frame (Case 1) showed approximately 3.85-times of the HS-20 truck. As the applied load increased to the ultimate capacity, a plastic strain appeared on the concrete deck, as shown in Figure 11a. High plastic strain developed above the top flange inside the intact girder along the span. This is attributed to the transverse bending of the deck to transfer the load from the fractured girder to the intact girder. Williamson et al. [11] reported that live loads applied to a fractured girder were transferred to an intact girder by transverse bending of the deck between the girders. In their full-scale bridge fracture test, they also found that the bending shape of the deck was initially a double curvature, which changed into a single curvature owing to the inside stud connection failure of the fractured girder along the span. Finally, the stud connection of the fractured girder failed along the span of the fractured girder, and the bridge collapsed. In the FE simulation, the stud connection failure of the bridge was initiated near the midspan and progressively developed into supports in the fractured girder as the applied live loads increased. As the applied load increased to the ultimate capacity, extensive stud connection failure occurred in the fractured girder along the span. Therefore, the deck acted as a cantilever supported along the inside top flange of the intact girder, and the pattern of the equivalent plastic strain conformed to this behavior.

As shown in Figure 11b, the plastic strain pattern of Case 2 was similar to that of Case 1; however, it was found that the high plastic strain spread more widely than in Case 1. The Von Mises equivalent stresses in Case 2 were comparable to those in Case 1, as shown in Figure 11c,d. In Case 1, the bottom flange of the intact girder was along the span. Compared with Case 1, the yielded region was widely distributed in Case 2, and more than half of the web yielded near the midspan. Based on the distributions of the plastic strains and Von Mises stresses, it can be inferred that the external cross-frame effectively contributed to load redistribution.



(**a**) Equivalent plastic strain (Case 1) (**b**) Equivalent plastic strain (Case 2)

(**c**) Von Mises equivalent stress (Case1) (**d**) Von Mises equivalent stress (Case2)

Figure 11. Equivalent plastic strain and Von Mises equivalent stress.

5. Summary and Conclusions

External cross-frames are utilized to increase the torsional resistance during the construction of a trapezoidal box-girder bridge. They are temporary members that are removed after a composite action in the bridge is achieved. Recent studies demonstrated that they can contribute to load redistribution as redundant sources [9,13]. In this study, the effectiveness of K-type external cross-frames as a redundant source was investigated. For this purpose, FE bridge models were constructed and the effects of the cross-frames were evaluated. The FE model was validated based on the results of a full-scale bridge fracture test conducted by Williamson et al. [11]. The load-displacement response of the FE model matched well with the test results, and the estimated ultimate capacity showed about a one percent difference compared to the test results.

Four different FE models (Cases 1 to 4) were constructed, depending on the presence of the external cross-frames and failure modes of the frame members considered in the analysis. In Case 1, external cross-frames were not incorporated into the bridge model. Possible failure modes, such as yielding and buckling of the frame members were considered in Case 2. To investigate the effects of the failure sequence of the frame members, the elastic behavior of the diagonals was assumed for Case 3 and the chords for Case 4. The ultimate capacities of the bridge models were evaluated by applying live loads after one of the two girders fractured. The axle configuration of an HS-20 truck load was utilized for live loads. The axle loads were modeled using point loads and placed above the damaged girder to maximize the live load effect.

The analysis results showed that the ultimate capacity of Case 1 was 3.85-times of the HS-20 truck. The load-displacement response of Case 2 showed a stiffer behavior than that of Case 1. The ultimate capacity of Case 2 was approximately 30% higher than that of Case 1. Case 3 exhibited a load-displacement response similar to that of Case 2, and the ultimate capacity was nine percent higher than that of Case 2. In Case 4, the ultimate capacity was similar to that of Case 1, but the load-displacement response exhibited an unstable behavior compared with the other cases. This was caused by the buckling of the external cross-frames.

From these results, it is concluded that external cross-frames can increase the stiffness and ultimate capacity of a bridge with one girder fracture. The external cross-frames contributed to the transverse redistribution of the applied live loads on the fractured girder. Therefore, external cross-frames can be considered a redundancy source. The failure

sequence of the frame members can affect the ultimate capacity and load-displacement response. It is not recommended to use a heavy section for chords, such that frame failure is initiated by the buckling of diagonals. In this study, only K-type external cross-frames were considered. Various factors, such as the frame type, location, connection, and number of frames, might affect the ultimate capacity of a bridge. Therefore, further research is required to utilize external cross-frames as reliable sources to increase bridge redundancy.

Author Contributions: J.K. performed FE simulations and wrote the draft for the article; B.W.K. gave advice on the simulations and the data analysis; S.K. supervised this research program and finalized the article. All authors have read and agreed to the published version of the manuscript.

Funding: This research was supported by Basic Science Research Program through the National Research Foundation of Korea (NRF) funded by the Ministry of Education (NRF-2021R1I1A3049510).

Institutional Review Board Statement: Not applicable.

Informed Consent Statement: Not applicable.

Data Availability Statement: Not applicable.

Conflicts of Interest: The authors declare no conflict of interest. The funders did not contribute to the study design; collection, analyses, or interpretation of data; writing of the manuscript; or decision to publish the results.

References

1. American Association of State Highway and Transportation Officials (AASHTO). *LRFD Bridge Design Specifications*, 9th ed.; AASHTO: Washington, DC, USA, 2020.
2. Connor, R.J.; Dexter, R.; Mahmoud, H. Inspection and Management of Bridges with Fracture-Critical Details. In *NCHRP Synthesis*; National Academy Press: Washington, DC, USA, 2005; Volume 354.
3. Fisher, J.W.; Pense, A.W.; Hausammann, H. Analysis of Cracking of I-79 Bridge at Neville Island. In *Fracture Problems in the Transportation Industry*; ASCE: New York, NY, USA, 1985; pp. 1–19.
4. Connor, R.J.; Kaufmann, E.J.; Fisher, J.W.; Wright, W.J. Prevention and Mitigation Strategies to Address Recent Brittle Fractures in Steel Bridges. *J. Bridge Eng.* **2007**, *12*, 164–173. [CrossRef]
5. Hesse, A.A.; Atadero, R.A.; Mahmoud, H.N. Approach-span failure of the Hoan Bridge as a case study for engineering students and practicing engineers. *J. Perform. Constr. Fac.* **2014**, *28*, 341–348. [CrossRef]
6. Hartle, R.A.; Amrhein, W.J.; Wilson, K.E., III; Baughman, D.R.; Tkacs, J.J. *Bridge Inspector's Training Manual/90*; FHWA-PD-91-015; FHWA: McLean, VA, USA, 1991.
7. Dexter, R.J.; Connor, R.J.; Mahmoud, H. Review of Steel Bridges with Fracture-Critical Elements. *Transp. Res. Rec.* **2005**, *1928*, 75–82. [CrossRef]
8. Hunley, C.T.; Harik, I.E. Structural Redundancy Evaluation of Steel Tub Girder Bridges. *J. Bridge Eng.* **2012**, *17*. [CrossRef]
9. Park, Y.; Joe, W.; Hwang, M.; Yoon, T. After-fracture redundancy in simple span two-girder steel bridge. *Struct. Eng. Mech.* **2007**, *27*, 651–670. [CrossRef]
10. Abedin, M.; Mehrabi, A.B. Effect of Cross-Frames on Load Distribution of Steel Bridges with Fractured Girder. *Infrastructures* **2020**, *5*, 32. [CrossRef]
11. Williamson, E.B.; Frank, K.H.; Samaras, V.A.; Kim, J.; Neuman, B.J.; Sutton, J.P.; Mouras, J.M.; Hovell, C.G.; Barnard, T. *Modeling the Response of Fracture Critical Steel Box-Girder Bridges*; Report 2010, FHWA/TX-08/0-5498-2; US Department of Commerce: Alexandria, VA, USA, 2010.
12. Samaras, V.A.; Sutton, J.P.; Williamson, E.B.; Frank, K.H. Simplified method for evaluating the redundancy of twin steel box-girder bridges. *J. Bridge Eng.* **2012**, *17*, 470–480. [CrossRef]
13. Pham, H.V.; Yakel, A.; Azizinamini, A. Experimental investigation of redundancy of twin steel box-girder bridges under concentrated loads. *J. Constr. Steel Res.* **2021**, *177*, 106440. [CrossRef]
14. Kim, K.; Yoo, C.H. Effects of external bracing on horizontally curved box girder bridges during construction. *Eng. Struct.* **2006**, *28*, 1650–1657. [CrossRef]
15. Shokouhian, M.; Shi, Y. Flexural strength of hybrid steel I-beams based on slenderness. *Eng. Struct.* **2015**, *93*, 114–128. [CrossRef]
16. Kim, J.; Williamson, E.B. Finite-element modeling of twin steel box-girder bridges for redundancy evaluation. *J. Bridge Eng.* **2015**, *20*, 04014106. [CrossRef]
17. Systemes, D. *ABAQUS Analysis User's Manual*, 12th ed.; Rising Sun Mills: Providence, RI, USA; ABAQUS Inc.: Palo Alto, CA, USA, 2012.
18. Linzell, D.G.; Nadakuditi, V.P. Parameters influencing seismic response of horizontally curved, steel, I-girder bridges. *Steel Compos. Struct.* **2011**, *11*, 21–38. [CrossRef]

19. Joo, H.S.; Moon, J.; Sung, I.; Lee, H. Moment redistribution of continuous composite I-girder with high strength steel. *Steel Compos. Struct.* **2015**, *18*, 873–887. [CrossRef]
20. Wu, J.; Frangopol, D.M.; Soliman, M. Simulating the construction process of steel-concrete composite bridges. *Steel Compos. Struct.* **2015**, *18*, 1239–1258. [CrossRef]
21. El-Zohairy, A.; Salim, H.; Shaaban, H.; Mustafa, S.; El-Shihy, A. Experimental and FE parametric study on continuous steel-concrete composite beams strengthened with CFRP laminates. *Constr. Build. Mater.* **2017**, *157*, 885–898. [CrossRef]
22. Kim, J.; Williamson, E.B. Ultimate behavior of stud connections within haunches. *J. Bridge Eng.* **2019**, *24*, 04018106. [CrossRef]
23. Mouras, J.M. Evaluating the Redundancy of Steel Bridges: Improving the Strength and Behavior of Shear Stud Connections under Tensile Loading. Master's Thesis, University of Texas at Austin, Austin, TX, USA, 2008.
24. Sutton, J.P.; Mouras, J.M.; Samaras, V.A.; Williamson, E.B.; Frank, K.H. Strength and ductility of shear studs under tensile loading. *J. Bridge Eng.* **2014**, *19*, 245–253. [CrossRef]
25. American Institute of Steel Construction. *Specification for Structural Steel Buildings*; AISC: Chicago, IL, USA, 2016.

Disclaimer/Publisher's Note: The statements, opinions and data contained in all publications are solely those of the individual author(s) and contributor(s) and not of MDPI and/or the editor(s). MDPI and/or the editor(s) disclaim responsibility for any injury to people or property resulting from any ideas, methods, instructions or products referred to in the content.